How to cite: *Angew. Chem. Int. Ed.* **2024**, *63*, e202318204
doi.org/10.1002/anie.202318204

Al-S Batteries

Locally Concentrated Ionic Liquid Electrolytes for Wide-Temperature-Range Aluminum-Sulfur Batteries

Cheng Xu, Thomas Diemant, Alessandro Mariani, Maria Enrica Di Pietro, Andrea Mele, Xu Liu, and Stefano Passerini**

Abstract: Aluminum–sulfur (Al–S) batteries are promising energy storage devices due to their high theoretical capacity, low cost, and high safety. However, the high viscosity and inferior ion transport of conventionally used ionic liquid electrolytes (ILEs) limit the kinetics of Al–S batteries, especially at sub-zero temperatures. Herein, locally concentrated ionic liquid electrolytes (LCILE) formed via diluting the ILEs with non-solvating 1,2-difluorobenzene (dFBn) co-solvent are proposed for wide-temperature-range Al–S batteries. The addition of dFBn effectively promotes the fluidity and ionic conductivity without affecting the $AlCl_4^-$/$Al_2Cl_7^-$ equilibrium, which preserves the reversible stripping/plating of aluminum and further promotes the overall kinetics of Al–S batteries. As a result, Al–S cells employing the LCILE exhibit higher specific capacity, better cyclability, and lower polarization with respect to the neat ILE in a wide temperature range from −20 to 40 °C. For instance, Al–S batteries employing the LCILE sustain a remarkable capacity of 507 mAh g^{-1} after 300 cycles at 20 °C, while only 229 mAh g^{-1} is delivered with the dFBn-free electrolyte under the same condition. This work demonstrates the favorable use of LCILEs for wide-temperature Al–S batteries.

Introduction

Since their commercialization in 1991, Li-ion batteries (LIBs) have been rapidly developed, conquering the market of portable electronics and electric vehicles to eventually become the most sold battery technology.[1–3] However, the potential cost increase due to limited supply of lithium, cobalt, and nickel has stimulated the interest for complementary and even alternative secondary batteries relying on more abundant elements.[4–6] Among them, rechargeable aluminum sulfur (Al–S) batteries employing high-abundant, low-cost, and high-capacity aluminum metal and sulfur as electrode materials are promising candidates.[7,8]

The current research on Al–S batteries is mainly focused on mitigating the polysulfide shuttle and promoting the sluggish conversion reaction of sulfur cathodes.[9–11] The proposed strategies of electrolyte additives,[12,13] sulfur host materials,[14–16] catalysts,[17–20] and functional separators have led to successfully prolonged lifespan and reduced cell polarization.[21] However, the inherent high viscosity and sluggish ion transport of conventionally employed electrolytes have not received attention from the scientific community. The state-of-the-art electrolytes for room-temperature rechargeable nonaqueous aluminum metal batteries are ionic liquid electrolytes (ILEs) consisting of 1-ethyl-3-methylimidazolium chloride (EmimCl) and aluminum chloride ($AlCl_3$).[22] The viscosity of $[EmimCl]_1[AlCl_3]_{1.5}$ is reported to be 19.4 mPa s at 20 °C,[23] while the electrolyte viscosity for commercial LIBs is usually lower than 10 mPa s.[24] The high viscosity hinders the penetration of electrolytes into thick electrodes, leading to a low utilization of sulfur encapsulated in porous host materials.[25] It is expected that this negative effect would become more pronounced at sub-zero temperatures due to the further decreased electrolyte fluidity. In fact, batteries that can operate at temperatures deviating from room temperature, e.g., −20&40 °C, are widely required even for civil use. Electrolyte engineering to decrease the electrolyte viscosity is a potential

[*] C. Xu, Dr. T. Diemant, Dr. X. Liu, Prof. S. Passerini
Helmholtz Institute Ulm (HIU) Electrochemical Energy Storage
Helmholtzstraße 11, D-89081 Ulm, Germany
E-mail: xu.liu@kit.edu
stefano.passerini@kit.edu
C. Xu, Dr. T. Diemant, Dr. X. Liu, Prof. S. Passerini
Karlsruhe Institute of Technology (KIT)
P.O. Box 3640, D-76021 Karlsruhe, Germany
Dr. A. Mariani
ELETTRA Sincrotrone Trieste
I-34012 Basovizza, Trieste, Italy
Dr. M. E. Di Pietro, Prof. A. Mele
Department of Chemistry
Materials and Chemical Engineering "Giulio Natta"
Politecnico di Milano
Piazza Leonardo da Vinci 32, Milan I-20133, Italy
Prof. S. Passerini
Chemistry Department
Sapienza University of Rome
Piazzale Aldo Moro 5, I-00185 Rome, Italy

approach to mitigate this issue. Moreover, a promoted electrolyte fluidity is usually accompanied with enhanced ion transport, which can contribute to lower cell polarization.

Adding low-viscosity cosolvents to ILEs is a feasible route to reduce viscosity and promote ion transport.[26,27] However, EmimCl-$AlCl_3$ binary ILEs with high Lewis acidity are highly reactive,[28] and the finely adjusted $AlCl_4^-$/$Al_2Cl_7^-$ equilibrium, essential for reversible aluminum stripping/plating, is rather sensitive to the electrolyte composition.[29] This leads to the difficulty in identifying suitable co-solvents. Recently, non-solvating and relatively inert co-solvents, e.g., 1,2-difluorobenzene (dFBn),[30] have been reported allowing to dilute high-viscosity concentrated electrolytes without affecting the local solvation of Li^+,[31–33] Na^+,[34] and K^+,[35] and forming the so-called locally concentrated electrolytes.[36,37] Even more recently, this strategy has been extended to concentrated electrolytes based on chemically stable ionic liquids.[38–43] Herein, the use of such emerging non-solvating co-solvents to $AlCl_3$-EmimCl binary ILEs to construct locally concentrated ionic liquid electrolytes (LCILEs) is explored to address the aforementioned issues. In fact, to the best of our knowledge, LCILEs for aluminum metal batteries have not been reported yet. Whether the unique $AlCl_4^-$/$Al_2Cl_7^-$ equilibrium is maintained in the presence of the non-solvating co-solvents and how the various co-solvent affects the LCILE performance is still unknown.

In particular, the most conventional, non-solvating co-solvent, i.e., dFBn, and the state-of-the-art ILE for aluminum metal batteries, i.e., $[EmimCl]_1[AlCl_3]_{1.3}$ (EA), are selected as model substances to evaluate their compatibility and to investigate the effect of LCILEs on the performance of Al–S batteries. It is anticipated that the addition of dFBn to EA effectively promotes the fluidity and ionic conductivity without affecting the $AlCl_4^-$/$Al_2Cl_7^-$ equilibrium, thus preserving the reversible stripping/plating of aluminum and promoting the overall kinetics of Al–S batteries. As a result, Al–S batteries employing LCILEs sustain a remarkable capacity of 507 mAh g^{-1} after 300 cycles at 20 °C, while only 229 mAh g^{-1} is delivered with the dFBn-free electrolyte under the same test conditions. Encouraged by the performance achieved at 20 °C, the electrochemical behavior at temperatures deviating from room temperature, e.g., −20, −10, and 40 °C, was also evaluated.

Results and Discussion

The LCILEs were prepared by mixing dFBn, $AlCl_3$, and EmimCl in the x:1.3:1 molar ratio (x = 0.4, 0.8, 1.2). These mixtures are named EAdF-x in the following. All the electrolytes are transparent without any phase separation or precipitation (Figure S1), which indicates that dFBn and EA are miscible in the chosen concentration range. The obtained electrolytes were then subjected to flashpoint tests. No flash is detected during the tests within the temperature range of 25–250 °C, proving their low flammability.

The viscosity of the electrolytes was measured via three parallel tests at 20 °C (Table S1), and the results are summarized in Figure 1a. As expected, the addition of dFBn into EA leads to a lower viscosity. For instance, the viscosity of EA and EAdF-1.2 are 18.5 and 4.9 mPa s, respectively. However, the ionic conductivity shows a maximum for x = 0.8 (20.2 mS cm^{-1}) as displayed in Figure 1b. The bell-shaped trend of the conductivity upon addition of dFBn is caused by the opposite effects of decreasing the number of charge carriers and viscosity. Nonetheless, all chosen LCILEs show higher ionic conductivity than the neat ILE, confirming that dFBn as a co-solvent effectively improves the fluidity and ion transport of EA electrolyte without compromising the low flammability.

As mentioned, the $AlCl_4^-$/$Al_2Cl_7^-$ equilibrium is crucial for the reversible stripping/plating of aluminum and conversion reaction of sulfur cathodes. Therefore, Raman spectra of the electrolytes and dFBn were measured to study the effect of dFBn on this equilibrium. The spectra of the electrolytes are normalized to the $AlCl_4^-$ peak at 349 cm^{-1}. As shown in Figure 1c, the intensity of the peak originating from dFBn at 296 cm^{-1} grows with its increased content.[44] Importantly, no obvious change of the position or normalized intensity of the peaks assigned to $AlCl_4^-$ (349 cm^{-1}) and $Al_2Cl_7^-$ (311 and 433 cm^{-1}) is observed for the electrolytes with different amount of dFBn, demonstrating that the cosolvent (dFBn) does not disturb the $AlCl_4^-$/$Al_2Cl_7^-$ equilibrium in all the electrolytes. Furthermore, ^{1}H NMR spectroscopy (Figure 1d) were carried out to reveal the change of the local chemical environment.[45] The peaks located at 6.43 and 6.48 ppm for EA correspond to the N–CH=CH–N protons of the imidazolium ring, while the dFBn signals in the region of 6.2–6.4 ppm can be attributed

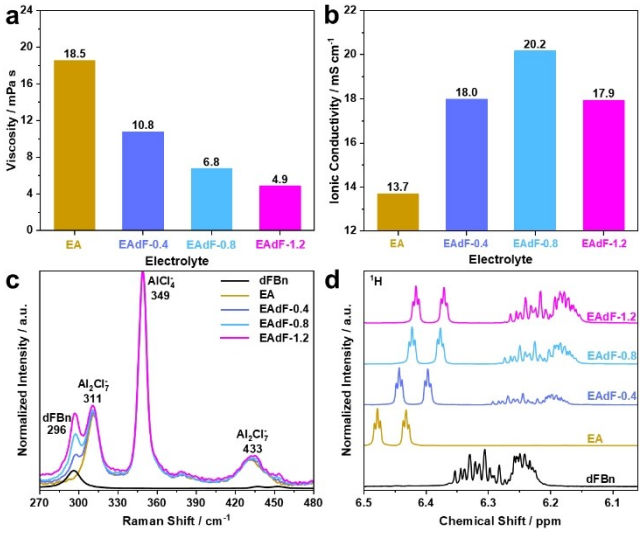

Figure 1. Physical properties and solvation characterization of the electrolytes at 20 °C. (a) Viscosity. (b) Ionic conductivity. (c) Raman spectra. The spectra of the electrolytes were normalized to the $AlCl_4^-$ peak at 349 cm^{-1}. (d) ^{1}H NMR spectra. The spectra of the electrolytes were normalized to the peak of the imidazolium proton appearing at 6.48 ppm in neat EA.

to the protons of the benzene ring. It is observed that the addition of dFBn to EA led to an upfield shift of all these peaks. These changes could be attributed to the interactions between $Emim^+$ and dFBn. In a previous work about Li^+-based LCILE, it is demonstrated that the charge transfer from $Emim^+$ to dFBn via their π–π stacking can lead to the shift in ^1H NMR spectra.[42] Therefore, the shift of the peaks observed in Figure 1d indicates for the interaction between $Emim^+$ and dFBn, confirming the miscibility of EA and dFBn.

Since EAdF-0.8 exhibits the highest ionic conductivity of the three LCILEs, it was selected as a model electrolyte to be compared with the neat ILE electrolyte, i.e., EA, in the following sections. The electrochemical properties of AMAs in these two electrolytes were evaluated in Al/Al symmetric cells at 20 °C. In the first step, Al/Al cells employing EA and EAdF-0.8 electrolytes were tested at various current densities to assess the rate capability. As shown in Figure 2a, the EA-based Al/Al cell exhibits a higher polarization compared with the EAdF-0.8 cell at the current densities from 0.1 to 1.0 mA cm^{-2}. Furthermore, the difference in the plateaus' average voltage increases from 10 mV at 0.1 mA cm^{-2} to 110 mV at 1 mA cm^{-2} (Figure 2b). The better rate capability achieved with EAdF-0.8 demonstrates a promoted kinetics of aluminum stripping/plating due to the presence of dFBn.

The cyclic stability of AMAs in EA and EAdF-0.8 electrolyte was further examined with Al/Al symmetric cells cycling at 0.054 mA cm^{-2} for 30 minutes in each step (cycled capacity of 0.27 mAh cm^{-2}), roughly corresponding to the current density and areal capacity of the Al–S cells later described. Apart from the lower cell polarization (Figure S2a), the use of EAdF-0.8 also leads to a longer lifespan. As shown in Figure S2b, a short circuit occurred after cycling for 760 h with EA electrolyte, while the cell employing EAdF-0.8 exhibited stable cycling for 1000 h, at least (Figure 2c). Figure 2d shows the electrochemical impedance spectra (EIS) of Al/Al cells employing EA and EAdF-0.8 recorded after 10 cycles. The high-frequency intercept corresponds to a pure resistor mainly reflecting the bulk resistance of the electrolyte. The depressed semicircle observed at lower frequencies, associated to the interfacial impedance, does not show obvious difference going from EA to EAdF-0.8 electrolyte, but the electrolyte bulk resistance with the latter electrolyte is much smaller. Therefore, the lower polarization of the Al/Al cell employing EAdF-0.8 mainly originates from the promoted ion transport in this electrolyte.

To understand the effect of dFBn on the morphology of the aluminum electrodes, scanning electron microscopy (SEM) was applied to cycled AMAs. More precisely, the electrodes were subjected to 20 galvanostatic cycles at 0.054 mA cm^{-2} up to an areal capacity of 0.27 mAh cm^{-2} at 20 °C. Then, the AMAs were extracted from the Al/Al cells and cleaned twice for 4 mins with dimethyl carbonate (DMC).

As shown in Figure 3a, the SEM image of the pristine AMA presents the typical texture of Al metal foil. After cycling, the surface morphology of both the AMAs exhibits obvious differences. The electrode cycled with EA shows

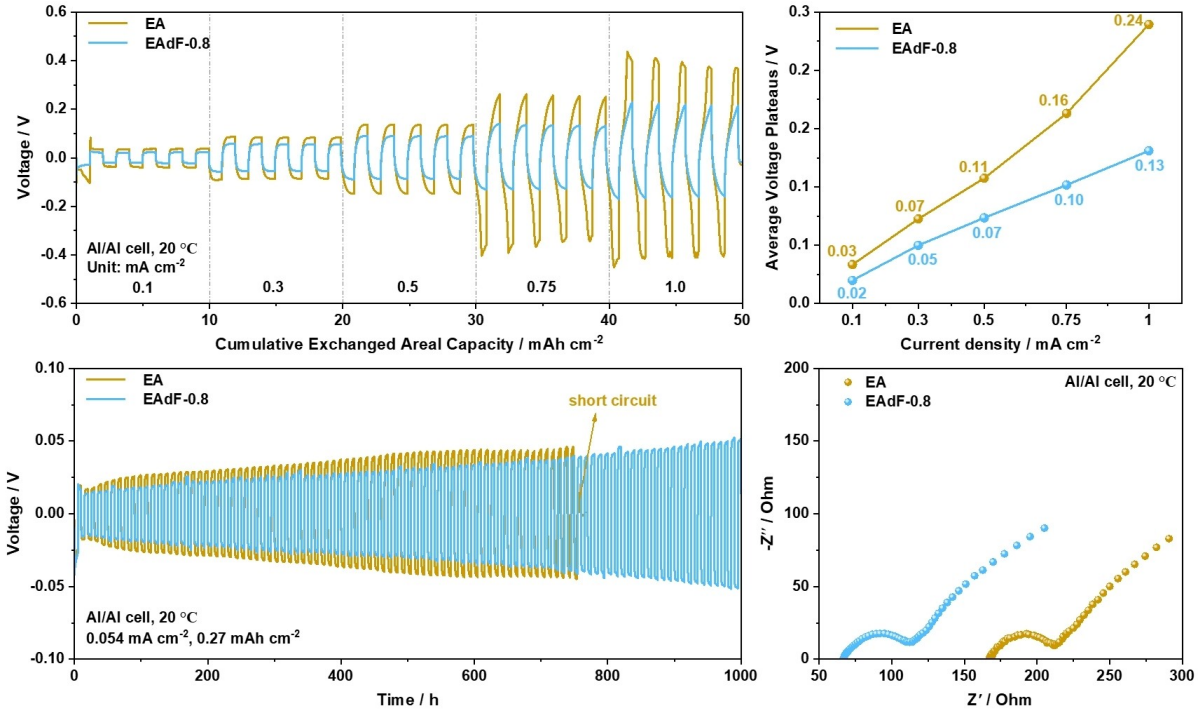

Figure 2. Electrochemical performance of Al/Al symmetric cells with EA and EAdF-0.8 electrolytes at 20 °C. (a) Voltage profiles and (b) corresponding average voltage plateaus of Al/Al cells at current densities of 0.1, 0.3, 0.5, 0.75 and 1 mA cm^{-2}. (c) Voltage profiles of Al/Al cells upon long-term cycling at 0.054 mA cm^{-2} with a capacity of 0.27 mAh cm^{-2}. (d) Nyquist plots of two-electrode Al/Al cells after cycling for 10 cycles.

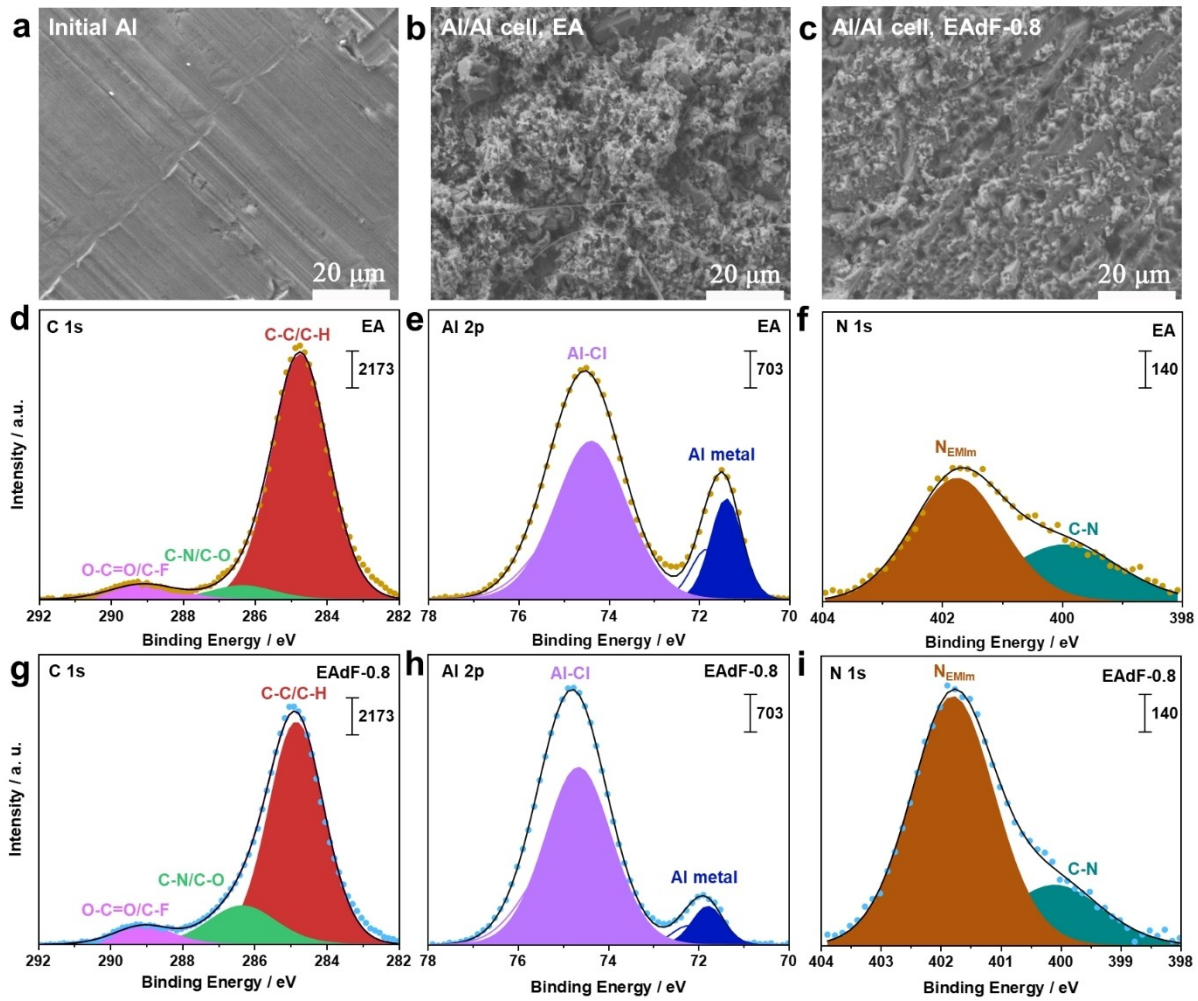

Figure 3. Surface morphology and SEI composition of AMAs after cycling in Al/Al cells for 20 cycles. SEM images of (a) initial Al metal, cycled Al anode in (b) EA and (c) EAdF-0.8 electrolytes. (d-i) XPS spectra of cycled AMAs in (d-f) EA and (g-i) EAdF-0.8 electrolytes.

the formation of larger particles and a more porous morphology (Figure 3b,c) with respect to that cycled with EAdF-0.8. Due to the uneven Al plating/stripping (Figure S3), the formed large deposits may penetrate the separator and ultimately lead to short circuit, in agreement with the result in Figure S2b. The same does not occur when adding dFBn into the electrolyte, resulting in a more uniform aluminum plating and stripping.

The solid electrolyte interphase (SEI) generated on AMAs is critical for their electrochemical behaviour. To understand the influence of dFBn on the SEI composition, cycled AMAs were analysed by X-ray photoelectron spectroscopy (XPS). The detail spectra in the C 1s range showed for both the AMAs cycled in EA (Figure 3d) and EAdF-0.8 (Figure 3g) a dominating peak due to C–C/C–H species at 284.8 eV. In addition, further peaks can be observed at 286.4 and 289.1 eV, which can be attributed to C–N/C–O and O–C=O/C–F groups, respectively. In the Al 2p range (Figure 3e,h), the peak doublets from metallic and oxidized Al, the latter most likely originating from Al–Cl bonds, can be discerned at 71.4 and 74.4 eV, respectively. The AMA cycled in EAdF-0.8 shows, however, a weaker Al metal peak, indicating that the addition of dFBn to the electrolyte promotes the formation of a thicker SEI layer. Two peaks are detected in the detail spectra in the N 1s region (Figure 3f,i) at 401.7 and 400.0 eV, which can be attributed to $Emim^+$ and C–N species (decomposition products of $Emim^+$), respectively. Comparison of the spectra indicates that the presence of dFBn promotes the contribution of $Emim^+$ to the SEI layer on the surface of AMAs. The Cl 2p and F 1s spectra as shown in Figure S4. While no obvious differences in peak position and intensity can be observed between the AMAs cycled in EA and EAdF-0.8, it was surprising to note that the F 1s spectrum of EA also showed signals of Al–F and C–F species at ~685.5 and ~688.0 eV (albeit with lower intensity). These latter might be caused by a slight corrosion of the PTFE cell body by the neat EA as PTFE is the only fluorine source in this cell (cf. Figure S4 for a more detailed discussion).

To explore the impact of dFBn on sulfur cathodes, Al–S batteries were assembled in three-electrode, T-shaped cells employing Al foils as counter and reference electrodes, and

graphene@S as the positive (cathode) electrode. Thermogravimetric analysis (TGA) reveals that the sulfur content of the synthesized graphene@S powders used for the electrodes are 34 and 54 wt % as shown in Figure S5. The corresponding sulfur loading of the cathodes is 0.5 and 1 mg cm^{-2}, respectively. SEM images in combination with energy dispersive X-ray (EDX) spectroscopy mapping of the graphene@S materials reveal in both cases a uniform distribution of sulfur in graphene@S (Figure S6).

Regarding the electrochemical performance, Figure 4a presents the evolution of the discharge specific capacity of Al–S cells employing graphene@S-34 % cathodes in EA and EAdF-0.8 electrolytes (the corresponding Coulombic efficiency are displayed in Figure S7) upon long-term cycling tests at 100 mA g^{-1} and 20 °C. The Al–S cells display an initial discharge specific capacity of 1511 and 1563 mAh g^{-1}, respectively, with EA and EAdF-0.8. After 300 cycles, the discharge specific capacity of the EAdF-0.8-based cell is 507 mAh g^{-1}, while it drops to 229 mAh g^{-1} for the cell employing EA. Additionally, the EAdF-0.8-based cell displays higher, although not close to 100%, Coulombic efficiency values. Hence, the cyclic stability of the Al–S cell using EAdF-0.8 electrolyte is greatly improved. Simultaneously, the dis-/charge polarization of Al–S cells is reduced via the addition of dFBn as shown in Figure 4b.

Al–S cells employing graphene@S-54 % cathodes were also assembled to further compare the performance of EAdF-0.8 and EA upon cycling at 50 mA g^{-1} (Figure 4c). Once more, the cyclability of the cells employing EAdF-0.8 is clearly better than those with EA. Specifically, an exemplary EAdF-0.8-based cell yields higher discharge specific capacity, i.e., 544 mAh g^{-1} after 40 cycles, than the EA-based cell (only 248 mAh g^{-1}) under the same test conditions. Similar to the results in Figure 4b, the Al–S cell using EAdF-0.8 shows a smaller redox polarization (Figure 4d). Cyclic voltammetry (CV) curves also confirm the polarization reduction in EAdF-0.8 electrolyte (Figure 4e). The enhanced cyclability and reduced polarization of the Al–S cells employing EAdF-0.8 prove the excellent compatibility of such an electrolyte with the S cathodes.

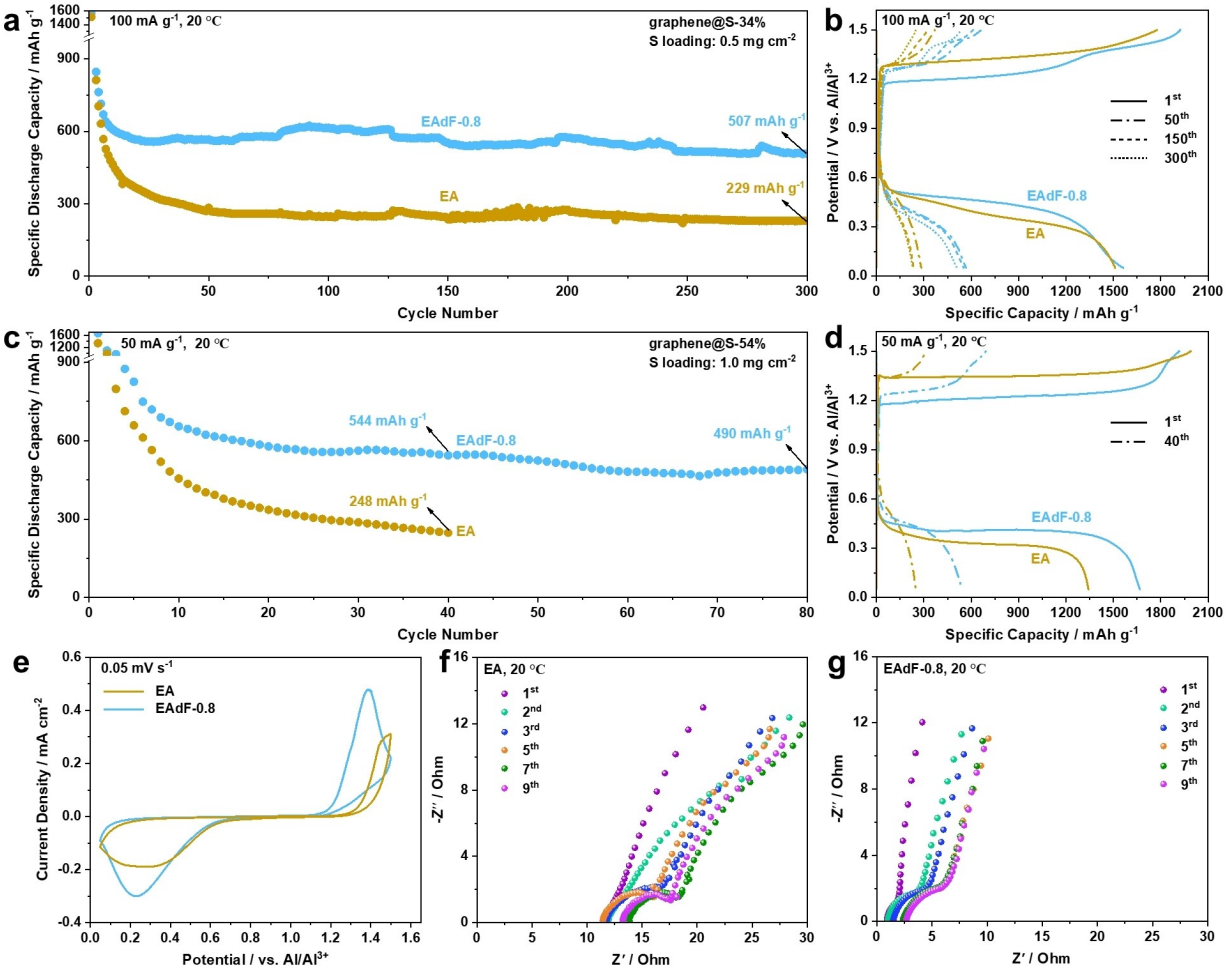

Figure 4. Electrochemical performance of Al–S cells with EA and EAdF-0.8 electrolytes at 20 °C. (a) Evolution of discharge specific capacity upon long-term dis-/charge cycling at the current density of 100 mA g^{-1}, and the corresponding (b) dis-/charge profiles at different cycles. (c) Evolution of discharge specific capacity upon long-term did-/charge cycling at the current density of 50 mA g^{-1}, and the corresponding (d) dis-/charge profiles. (e) CV curves at a scan rate of 0.05 mV s^{-1}. (f, g) Nyquist plots of cycled three-electrode Al-S cells at different cycle in EA (f) and EAdF-0.8 (g) electrolyte.

To reveal the mechanism of such improvements, EIS of Al–S cells was performed in a first step. As exhibited in Figure 4f,g, the Nyquist plot of the sulfur cathodes of three-electrode Al-S cells in EAdF-0.8 shows lower bulk resistance and interfacial impedance, indicating a higher ionic conductivity (in accordance with Figure 1a) and promoted interfacial reaction in the dFBn-containing electrolyte. The impedance of the Al–S cell employing EAdF-0.8 initially increases to stabilize after 7 cycles. On the other hand, the impedance of the EA-based cell is much higher and does not reach stability. This indicates that a stable cathode/electrolyte interphase (CEI) is gradually forming during the first few cycles in EAdF-0.8, which is not the case for the EA-based cell.

In a further step, SEM and XPS measurements were carried out with cathodes in the fully charged state to explore the surface morphology and CEI compositions after cycling. The comparison of the SEM images of graphene@S cathodes pristine (Figure 5a) and after cycling in EA and EAdF-0.8 (Figure 5b,c respectively) does not show obvious changes. However, EDX detects signals of C, Al, Cl, N, S, O and F on the surface of the cycled cathodes (Figure S8), indicating the presence of the CEI.

Figure 5d–i shows the XPS spectra of graphene@S cathodes recovered after cycling in EA and EAdF-0.8 electrolyte. First of all, comparison of the spectra in the Al 2p and Cl 2p regions (Figure 5d,e,g,h) showed a much smaller concentration of Al–Cl species after cycling with EAdF-0.8. Furthermore, according to the N 1s spectra (Figure S9b,e), the electrode cycled in EAdF-0.8 exhibited also less N_{EMIm} and more C–N species. The S 2p spectra of the sulfur cathode cycled in EA (Figure 5f) showed three peak doublets which can be assigned to monosulfide S^{2-} (S 2p3/2 peak at 160.9 eV), disulfide S_2^{2-}/terminal S atoms in polysulfides (162.0 eV), and internal S atoms of polysulfides/elemental S species (163.5 eV), respectively.[46] With the presence of dFBn in the electrolyte (EAdF-0.8) (Figure 5i), a weaker disulfide/terminal polysulfide signal was observed while the monosulfide peak doublet vanished completely. Since the electrodes were at the fully charged state, the lower intensity of the signals of reduced S species points to a promoted reconversion of S in EAdF-0.8. The overall higher intensity of the S 2p spectra of the cathode cycled in EA with respect to the one in EAdF-0.8 demonstrates a higher S content in the former electrode. Correlating this with the electrochemical results, one can infer that this is caused by a

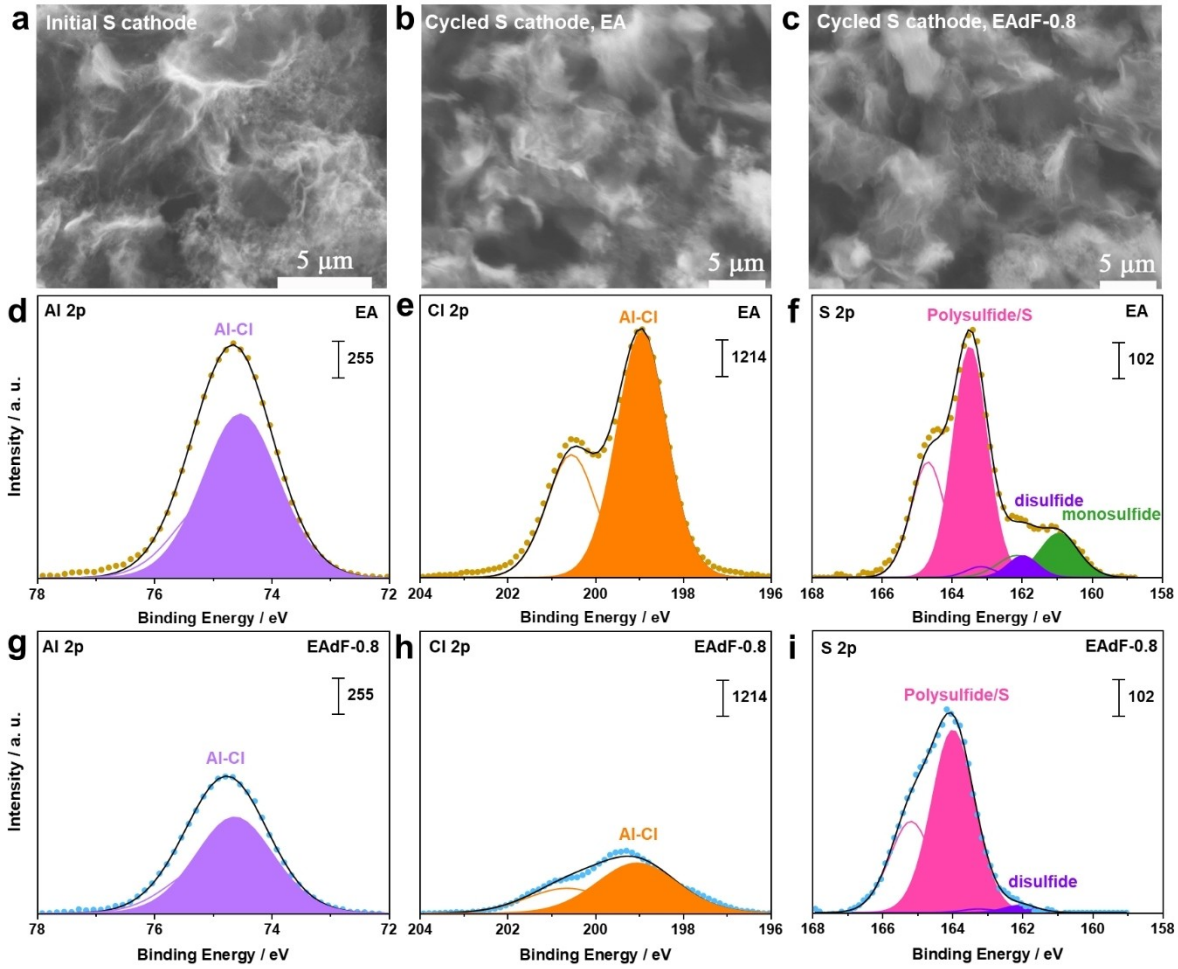

Figure 5. Surface morphology and CEI composition of sulfur cathodes after cycling for 50 cycles. SEM images of (a) initial S cathode, cycled S cathode in (b) EA and (c) EAdF-0.8 electrolytes. (d-i) XPS spectra of cycled S cathode in (d–f) EA and (g–i) EAdF-0.8 electrolytes.

lower sulfur utilization in EA due to its higher viscosity. Finally, similar to the findings for the AMAs (Figure S4c), fluorine was not only detected for the cathode tested in EAdF-0.8, but also for the EA one (Figure S9c). This is most probably again caused by the slight corrosion of the PTFE cell.

The above results demonstrate that EAdF-0.8 effectively promotes the electrochemical performance of Al–S cells at 20 °C due to its enhanced fluidity, ion transport, and compatibility toward AMAs and sulfur cathodes. In a further step, we proceeded to explore its use for Al–S batteries in a wider temperature range.

The physical properties of the electrolytes at a wide temperature range are firstly compared. Figure 6a shows the differential scanning calorimetry (DSC) spectra of EA and EAdF-0.8 electrolytes. In the cooling trace, a crystallization peak (Tc) is observed on both electrolytes, but Tc of EAdF-0.8 is shifted to lower temperatures, being very close to that of dFBn (Figure S10). In the heating trace, a cold-recrystallization feature, Tc', is detected only for EAdF-0.8. Additionally, compared with EA, EAdF-0.8 presents a lower melting peak (Tm). These results demonstrate that the addition of dFBn into EA leads to a much wider liquidus range. The ionic conductivities of EA and EAdF-0.8 electrolyte were measured in a temperature range from −30 to 50 °C (Figure 6b). As displayed, dFBn effectively enhances the ionic mobility over the tested temperature range. EA shows a sharp decline when the temperature is below −10 °C, corresponding to its freezing point (Figure 6a). Due to the extended liquidus range with the presence of dFBn, such a sharp decrease of ionic conductivity is not observed for EAdF-0.8. Specifically, at −20 °C, EAdF-0.8 has a significantly higher ionic conductivity (6.64 mS cm^{-1}) than EA (0.42 mS cm^{-1}). Figure 6c displays the Raman spectra of both the electrolytes collected at −20, −10, and 40 °C. In general, the peaks of $AlCl_4^-$ and $Al_2Cl_7^-$ do not show obvious change in this temperature range, which indicates the preserved $AlCl_4^-/Al_2Cl_7^-$ equilibrium. The Raman spectra of the electrolytes in a wider temperature range, i.e., from −80 to 60 °C, are shown in Figure S11. Despite the occurrence of crystallization, the $AlCl_4^-/Al_2Cl_7^-$ equilibrium does not appear to be significantly affected.

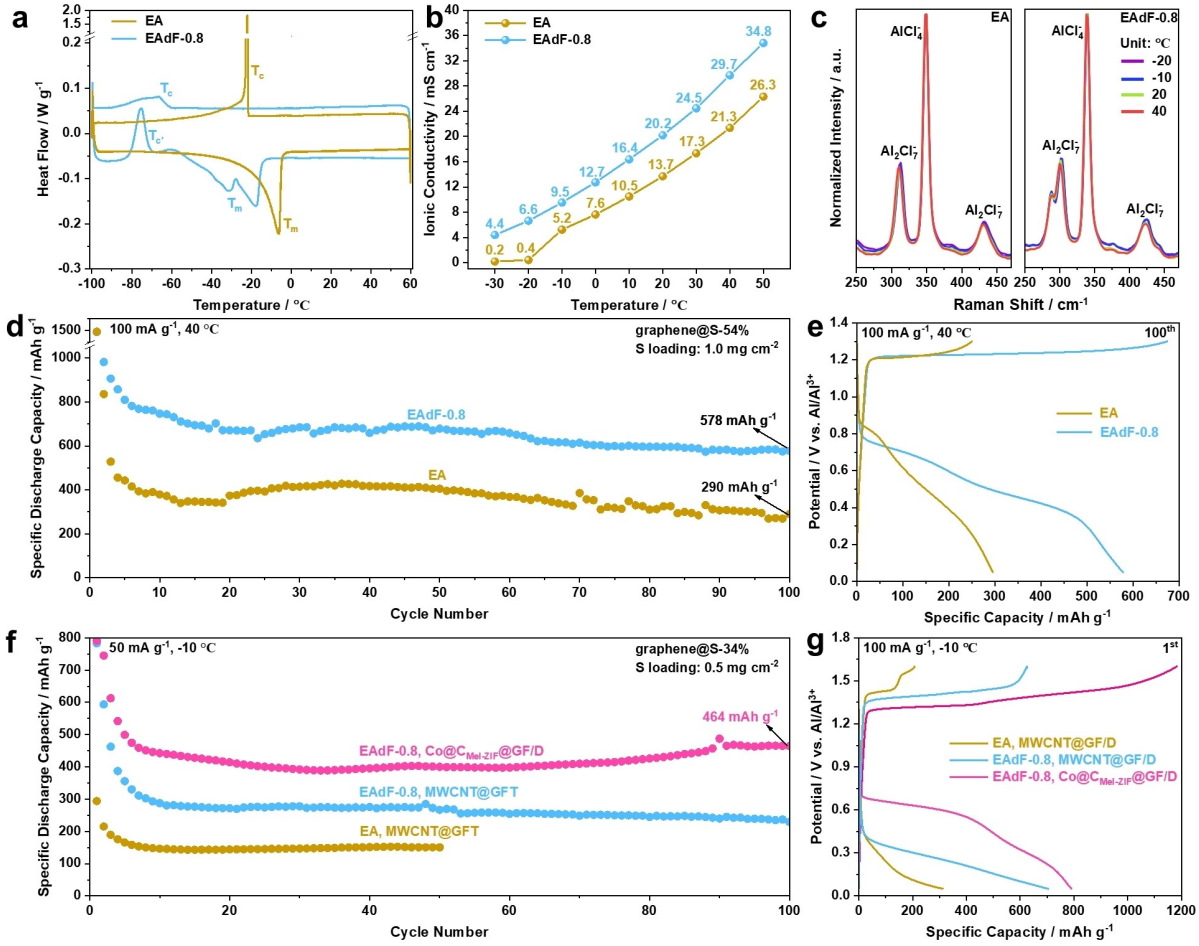

Figure 6. Physical properties of EA and EAdF-0.8 in a wide temperature range, and the electrochemical performance of Al–S cells with EA and EAdF-0.8 at varying temperatures between −20 and 40 °C. (a) DSC thermogram with a sweep rate of 5 °C min^{-1}. (b) Ionic conductivity between −30–50 °C. (c) Raman spectra at −20, −10, 20 and 40 °C. The spectra were normalized to the $AlCl_4^-$ peak at 349 cm^{-1}. (d) The discharge specific capacity upon long-term cycling at 100 mA g^{-1} and 40 °C, and corresponding (e) dis-/charge profiles. (f) The discharge specific capacity upon long-term cycling at 50 mA g^{-1} and −10 °C, and corresponding (g) dis-/charge profiles.

Figure 6d displays the discharge specific capacities of Al–S cell employing graphene@S-54 % cathode upon long-term cycling at 100 mA g^{-1} and 40 °C. The EAdF-0.8 based Al–S cell exhibits an initial specific capacity of 1495 mAh g^{-1} and maintained 578 mAh g^{-1} at the 100th cycle. In contrast, the specific capacity of the EA based Al–S cell decreases from 1494 to 290 mAh g^{-1} after 100 cycles. Meanwhile, the Al–S cell using EAdF-0.8 displays a lower polarization (Figure 6e).

Figure 6f shows the evolution of discharge specific capacities upon long-term cycling of Al–S cells employing graphene@S-34 % cathode at 50 mA g^{-1} and −10 °C. The cells based on EA and EAdF-0.8 deliver initial specific capacities of 294 and 782 mAh g^{-1}, respectively. The lower initial discharge specific capacities are caused by the lower ionic conductivity and higher viscosity, which decreases the overall kinetics of the cells upon dis-/charge. Nonetheless, the EAdF-0.8 cell displays a much lower decrease. In order to promote the reaction kinetics, other strategies are required to further improve the performance at such low temperatures. Recently, our group reported a low-polarization and long-lifespan Al–S batteries in which the kinetics was improved by a separator modified with a layer of 3D nitrogen-doped carbonaceous networks anchored with cobalt, namely, Co@$C_{Mel\text{-}ZIF}$@GF/D.[47] Herein, this modified separator is combined with the Al/EAdF-0.8/S cells for the electrochemical tests at low temperatures. With this modified separator, the polarization is effectively reduced (Figure 6g) and the capacity at the 100th cycle is improved to 464 mAh g^{-1} even at −10 °C.

Finally, Al/Al symmetric cells employing either EA or EAdF-0.8 were tested at −20 °C (Figure S12). The use of EAdF-0.8 enables Al/Al cells with a good rate capability up to 0.2 mA cm^{-2} and long-term cycling for 800 h, which demonstrates the possible use of this electrolyte for low temperature aluminum metal batteries. The evolution of discharge specific capacities upon long-term cycling of Al–S cells with graphene@S-34 % cathode at 20 mA g^{-1} and −20 °C is displayed in Figure S13. For the cell employing the neat EA, the specific discharge capacity is only 84 mAh g^{-1} at the 100th cycle. When EAdF-0.8 is combined with a Co@$C_{Mel\text{-}ZIF}$@GF/D separator, lower polarization and an even better cyclability are achieved (Figure S13). The capacity after cycling 100 cycles was 283 mAh g^{-1} in these experimental conditions, being among the best performance reported in literature (Table S2). These results demonstrate the promoted kinetics of the Al–S batteries at low temperatures resulting from the use of dFBn as electrolyte co-solvent.

Conclusion

In summary, the addition of dFBn to EA effectively promotes the fluidity and ionic conductivity without affecting the $AlCl_4^-/Al_2Cl_7^-$ equilibrium, thus preserving the reversible stripping/plating of aluminum and further promoting the overall kinetics of Al–S batteries. As a result, Al–S cells employing the EAdF-0.8 exhibit higher specific capacity, better cyclability, and lower polarization with respect to those based on the neat EA in a wide temperature range from −20 to 40 °C. Moreover, the combination of the EAdF-0.8 with a modified separator can further promote the specific capacity at low temperatures. Overall, these results demonstrate the benefits resulting from the rational design of EAdF-0.8 consisting of EA and dFBn for wide-temperature range Al–S batteries.

Acknowledgements

This work was supported by the China Scholarship Council (CSC); the Helmholtz Association Basic funding; and the postdoctoral fellowship in the framework of the "MSCA EF Master Class 2018" funding programme in the Politecnico di Milano. Open Access funding enabled and organized by Projekt DEAL.

Conflict of Interest

The authors declare no conflict of interest.

Data Availability Statement

The data that support the findings of this study are available on request from the corresponding author. The data are not publicly available due to privacy or ethical restrictions.

Keywords: Aluminum sulfur batteries · non-solvating co-solvent · locally concentrated electrolytes · ionic liquid electrolytes · wide temperature range

[1] B. Dunn, H. Kamath, J. M. Tarascon, *Science* **2011**, *334*, 928–935.
[2] J. M. Tarascon, M. Armand *Nature* **2001**, *414*, 359–367.
[3] J. B. Goodenough, K. S. Park, *J. Am. Chem. Soc.* **2013**, *135*, 1167–1176.
[4] M. Li, J. Lu, Z. Chen, K. Amine, *Adv. Mater.* **2018**, *30*, 1800561.
[5] H. Kim, G. Jeong, Y. U. Kim, J. H. Kim, C. M. Park, H. J. Sohn, *Chem. Soc. Rev.* **2013**, *42*, 9011–9034.
[6] F. Degen, M. Winter, D. Bendig, J. Tübke, *Nat. Energy* **2023**, *8*, 1284–1295.
[7] Q. Pang, J. Meng, S. Gupta, X. Hong, C. Y. Kwok, J. Zhao, Y. Jin, L. Xu, O. Karahan, Z. Wang, S. Toll, L. Mai, L. F. Nazar, M. Balasubramanian, B. Narayanan, D. R. Sadoway, *Nature* **2022**, *608*, 704–711.
[8] H. Li, R. Meng, Y. Guo, B. Chen, Y. Jiao, C. Ye, Y. Long, A. Tadich, Q. H. Yang, M. Jaroniec, S. Z. Qiao, *Nat. Commun.* **2021**, *12*, 5714.
[9] Q. Zhou, Y. Wu, J. Gautam, D. Wang, X. Jiang, Z. Ma, H. Zhang, L. Ni, G. Diao, *Coord. Chem. Rev.* **2023**, *474*, 214856.
[10] M. Klimpel, M. V. Kovalenko, K. V. Kravchyk, *Commun. Chem.* **2022**, *5*, 77.
[11] J. Zhang, R. He, L. Jia, C. You, Y. Zhang, M. Liu, N. Tian, H. Lin, J. Wang, *Adv. Funct. Mater.* **2023**, *33*, 2305674.
[12] X. Yu, M. J. Boyer, G. S. Hwang, A. Manthiram, *Chem* **2018**, *4*, 586–598.

[13] C. Xu, T. Diemant, X. Liu, S. Passerini, *Adv. Funct. Mater.* **2023**, *33*, 2214405.
[14] Y. Guo, H. Jin, Z. Qi, Z. Hu, H. Ji, L. J. Wan, *Adv. Funct. Mater.* **2019**, *29*, 1807676.
[15] Y. Zhang, L. Ma, R. Tang, X. Zheng, X. Wang, Y. Dong, G. Kong, F. Zhao, L. Wei, *Int. J. Hydrogen Energy* **2021**, *46*, 4936–4946.
[16] X. Xiao, J. Tu, Z. Huang, S. Jiao, *Phys. Chem. Chem. Phys.* **2021**, *23*, 10326–10334.
[17] Y. Guo, Z. Hu, J. Wang, Z. Peng, J. Zhu, H. Ji, L. Wan, *Angew. Chem. Int. Ed.* **2020**, *132*, 23163–23167.
[18] Z. Lin, M. Mao, T. Lv, S. Li, Y. S. Hu, H. Li, X. Huang, L. Chen, L. Suo, *Energy Storage Mater.* **2022**, *51*, 266–272.
[19] Z. Huang, W. Wang, W. L. Song, M. Wang, H. Chen, S. Jiao, D. Fang, *Angew. Chem. Int. Ed.* **2022**, *61*, e202202696.
[20] S. Ju, J. Ye, H. Zhang, W. Wang, G. Xia, W. Cui, Y. Yang, H. Pan, X. Yu, *Energy Storage Mater.* **2023**, *56*, 1–12.
[21] F. Wang, M. Jiang, T. Zhao, P. Meng, J. Ren, Z. Yang, J. Zhang, C. Fu, B. Sun, *Nano-Micro Lett.* **2022**, *14*, 169.
[22] M. C. Lin, M. Gong, B. Lu, Y. Wu, D. Y. Wang, M. Guan, M. Angell, C. Chen, J. Yang, B. J. Hwang, H. Dai, *Nature* **2015**, *520*, 325–328.
[23] G. A. Elia, K. Hoeppner, R. Hahn, *Batteries & Supercaps* **2021**, *4*, 368–373.
[24] C. Sauter, R. Zahn, V. Wood, *J. Electrochem. Soc.* **2020**, *167*, 100546.
[25] H. Li, J. Lampkin, N. Garcia-Araez, *ChemSusChem* **2021**, *14*, 3139–3146.
[26] R. S. Kühnel, N. Böckenfeld, S. Passerini, M. Winter, A. Balducci, *Electrochim. Acta* **2011**, *56*, 4092–4099.
[27] U. Pal, D. Rakov, B. Lu, B. Sayahpour, F. Chen, B. Roy, D. R. MacFarlane, M. Armand, P. C. Howlett, Y. S. Meng, M. Forsyth, *Energy Environ. Sci.* **2022**, *15*, 1907–1919.
[28] G. A. Elia, J. B. Ducros, D. Sotta, V. Delhorbe, A. Brun, K. Marquardt, R. Hahn, *ACS Appl. Mater. Interfaces* **2017**, *9*, 38381–38389.
[29] Y. Zhang, S. Liu, Y. Ji, J. Ma, H. Yu, *Adv. Mater.* **2018**, *30*, 1706310.
[30] D. J. Yoo, S. Yang, K. J. Kim, J. W. Choi, *Angew. Chem. Int. Ed.* **2020**, *59*, 14869–14876.
[31] C. Zhu, C. Sun, R. Li, S. Weng, L. Fan, X. Wang, L. Chen, M. Noked, X. Fan, *ACS Energy Lett.* **2022**, *7*, 1338–1347.
[32] N. Piao, X. Ji, H. Xu, X. Fan, L. Chen, S. Liu, M. N. Garaga, S. G. Greenbaum, L. Wang, C. Wang, X. He, *Adv. Energy Mater.* **2020**, *10*, 1903568.
[33] Z. Jiang, Z. Zeng, X. Liang, L. Yang, W. Hu, C. Zhang, Z. Han, J. Feng, J. Xie, *Adv. Funct. Mater.* **2021**, *31*, 2005991.
[34] J. Zheng, S. Chen, W. Zhao, J. Song, M. H. Engelhard, J. G. Zhang, *ACS Energy Lett.* **2018**, *3*, 315–321.
[35] L. Qin, N. Xiao, J. Zheng, Y. Lei, D. Zhai, Y. Wu, *Adv. Energy Mater.* **2019**, *9*, 1902618.
[36] X. Cao, H. Jia, W. Xu, J.-G. Zhang, *J. Electrochem. Soc.* **2021**, *168*, 010522.
[37] L. Tan, S. Chen, Y. Chen, J. Fan, D. Ruan, Q. Nian, L. Chen, S. Jiao, X. Ren, *Angew. Chem. Int. Ed.* **2022**, *61*, e202203693.
[38] S. Lee, K. Park, B. Koo, C. Park, M. Jang, H. Lee, H. Lee, *Adv. Funct. Mater.* **2020**, *30*, 2003132.
[39] X. Liu, A. Mariani, H. Adenusi, S. Passerini, *Angew. Chem. Int. Ed.* **2023**, *62*, e202219318.
[40] Z. Wang, F. Zhang, Y. Sun, L. Zheng, Y. Shen, D. Fu, W. Li, A. Pan, L. Wang, J. Xu, J. Hu, X. Wu, *Adv. Energy Mater.* **2021**, *11*, 2003752.
[41] Y. Cai, Q. Zhang, Y. Lu, Z. Hao, Y. Ni, J. Chen, *Angew. Chem. Int. Ed.* **2021**, *60*, 25973–25980.
[42] X. Liu, A. Mariani, T. Diemant, M. E. Di Pietro, X. Dong, M. Kuenzel, A. Mele, S. Passerini, *Adv. Energy Mater.* **2022**, *12*, 2200862.
[43] X. Liu, A. Mariani, T. Diemant, X. Dong, P. H. Su, S. Passerini, *Angew. Chem. Int. Ed.* **2023**, *135*, e202305840.
[44] X. Wen, Y. Liu, A. Jadhav, J. Zhang, D. Borchardt, J. Shi, B. M. Wong, B. Sanyal, R. J. Messinger, J. Guo, *Chem. Mater.* **2019**, *31*, 7238–7247.
[45] C. Ferrara, V. Dall'Asta, V. Berbenni, E. Quartarone, P. Mustarelli, *J. Phys. Chem. C* **2017**, *121*, 26607–26614.
[46] X. Liu, T. Diemant, A. Mariani, X. Dong, M. E. Di Pietro, A. Mele, S. Passerini, *Adv. Mater.* **2022**, *34*, 2207155.
[47] C. Xu, M. Zarrabeitia, Y. L. Li, J. Biskupek, U. Kaiser, X. Liu, S. Passerini, *ACS Nano* **2023**, *17*, 25234–25242.

Manuscript received: November 28, 2023
Accepted manuscript online: January 20, 2024
Version of record online: January 31, 2024